International Journal of Nanomedicine

Dovepress

open access to scientific and medical research

Open Access Full Text Article

ORIGINAL RESEARCH

A Glutathione-Consuming Bimetallic Nano-Bomb with the Combination of Photothermal and Chemodynamic Therapy for Tumors: An in vivo and in vitro Study

Jing Kong[1,*], Jiabin Lai[2–4,*], Min Wang[5,*], Yi Xie[1], Haifei He[6], Jiayu Gu[7], Tao Pan[6], Zhiqiang Lu[8], Lifeng Jiang[3,4]

[1]Department of Endocrinology and Metabolism, The Second Affiliated Hospital, Zhejiang University School of Medicine, Hangzhou, People's Republic of China; [2]Department of Pathology, The Second Affiliated Hospital, Zhejiang University School of Medicine, Hangzhou, People's Republic of China; [3]Department of Orthopedic Surgery, The Second Affiliated Hospital, Zhejiang University School of Medicine, Orthopedic Research Institute of Zhejiang University, Hangzhou, People's Republic of China; [4]Key Laboratory of Motor System Disease Research and Precision Therapy of Zhejiang Province, Clinical Research Center of Motor System Disease of Zhejiang Province, Hangzhou, People's Republic of China; [5]Digestive Endoscopy Department, The First Affiliated Hospital with Nanjing Medical University & Jiangsu Province Hospital, Nanjing, People's Republic of China; [6]Department of Breast Surgery and Oncology, Key Laboratory of Cancer Prevention and Intervention, Ministry of Education, The Second Affiliated Hospital, Zhejiang University School of Medicine, Hangzhou, People's Republic of China; [7]Jiangsu Institute of Metrology, Nanjing, People's Republic of China; [8]Department of Oncology, Zhongda Hospital, School of Medicine, Southeast University, Nanjing, People's Republic of China

*These authors contributed equally to this work

Correspondence: Lifeng Jiang; Zhiqiang Lu, Email jianglifeng@zju.edu.cn; taiyi1981@126.com

Background: Chemodynamic therapy (CDT) faces challenges of low catalytic ion efficiency and ROS production. We developed a ROS nano-bomb, Cu/ZIF-8@GA-Fe, to address these issues.

Methods: The nano-bomb was synthesized by doping copper into ZIF-8 and assembling Fe^{3+} and gallic acid (GA). It was tested for reactive oxygen species (ROS) generation in acidic conditions and its photothermal properties.

Results: In an acidic micro environment, Cu/ZIF-8@GA-Fe effectively released Fe^{3+} and Cu^{2+}, depleting GSH and generating ROS. The GA-Fe coating provided photothermal heat and was used to enhance Fenton reactions via dual ions for increasing ROS production. In vivo and in vitro experiments, Cu/ZIF-8@GA-Fe inhibited tumor growth with minimal side effects.

Conclusion: Cu/ZIF-8@GA-Fe shows promise for safe and effective CDT, offering a synergistic approach to tumor therapy.

Keywords: reactive oxygen species, nano-bomb, combination therapy, chemodynamic therapy, photothermal therapy

Introduction

Reactive oxygen species (ROS)-based therapies have garnered significant attention for their high efficacy and limited drug resistance in the treatment of cancers.[1–3] Traditional ROS therapies such as photodynamic therapy (PDT)[4,5] and sonodynamic therapy (SDT)[6,7] are subject to certain limitations, including hypoxia and limited penetration depth of the light source. Recently, chemodynamic therapy (CDT) harnesses the Fenton/Fenton-like reaction to catalyze the production of highly toxic •OH from hydrogen peroxide, effectively targeting malignancies for eradication.[8–11] Furthermore, cancer cells exhibit heightened vulnerability to oxidative damage compared to healthy cells. ROS instigate oxidative stress, disrupt redox homeostasis, and ultimately culminate in therapeutic outcomes.[12–16] Despite CDT's independence from oxygen levels or light sources, debates persist regarding its therapeutic efficacy. This discourse is amplified by the substantial presence of the adaptive antioxidant glutathione (GSH) and the constrained catalytic activity inherent in the Fenton or Fenton-like processes, both of which undermine CDT's effectiveness.[17–21] Consequently, there is an imperative to devise innovative strategies aimed at augmenting the therapeutic potential of CDT.

Received: 30 April 2024
Accepted: 7 August 2024
Published: 21 August 2024

There is accumulating evidence that intracellular GSH plays a pivotal role in scavenging ROS to maintain redox homeostasis, thereby markedly attenuating the toxicity of •OH to cancer cells.[3] During the utilization of Fenton or Fenton-like processes, various metal ions in elevated valence states, particularly Cu^{2+}, Fe^{3+}, and Mn^{4+}, are frequently utilized to deplete GSH, subsequently undergoing reduction to low valence states.[22] While single metal ion-mediated CDT presents robust anti-tumor therapeutic benefits, it is not devoid of limitations. For instance, the efficient execution of the Fenton reaction with Fe^{2+} necessitates strongly acidic conditions, typically within the pH range of 2–4, thereby restricting the therapeutic efficiency of monometallic ion-mediated CDT, particularly in slightly acidic tumor microenvironments.[8] Consequently, to enhance the therapeutic efficacy of CDT, dual metal ion redox pairs can be incorporated into anti-tumor CDT materials. Among these, bimetallic elements based on copper/iron have garnered widespread utilization.[23–25] For instance, Wang et al synthesized hemoglobin (Hb)-functionalized copper ferrite nanoparticles (Hb-CFNPs) and employed the CDT/photothermal therapy (PTT) system to augment CDT efficacy.[26] The redox pairings Fe^{2+}/Fe^{3+} and Cu^{+}/Cu^{2+} in CFNPs facilitated the conversion of H_2O_2 to •OH via Fenton and Fenton-like reactions (CDT effect). Nonetheless, such techniques are imperative for the advancement of CDT, as bimetallic-mediated CDT solutions remain scarce.

PTT, capable of converting near-infrared (NIR) light energy into heat, emerges as a promising alternative to established anticancer modalities owing to its minimally invasive nature, limited damage to normal tissues, and precise spatial and temporal control.[27–29] The heat generated by PTT induces protein denaturation and disruption of the cell membrane, ultimately leading to the demise of tumor cells. PTT is highly effective in treating deep tumors because the laser can penetrate tissues and directly target tumor cells. Some tumors exhibit resistance to conventional treatments, but PTT, as an innovative approach, offers potential advantages for treating drug-resistant tumors. Furthermore, this heat accelerates the Fenton reaction, thereby enhancing its anticancer efficacy.[30,31] Consequently, the synergistic effects of PTT and CDT represent a compelling research avenue in tumor therapy. To achieve such goal, researchers have explored various materials. For example, studies have demonstrated that gallic acid (GA), a naturally occurring polyhydroxyphenolic molecule, readily forms complexes with Fe^{3+} to generate compatibilizers with favorable photothermal conversion properties. Consequently, GA-Fe^{3+} coordination polymers emerge as promising iron sources for CDT applications.[22]

In the present study, we engineered a GSH-consuming bimetallic nano-bomb for the combined CDT/PTT therapy for tumors. As depicted in Scheme 1, Cu/ZIF-8 NPs were synthesized in a single step via a facile ion doping method, followed by the in-situ assembly of GA and Fe^{3+} on the surface of Cu/ZIF-8 to form nanocomposites (Cu/ZIF-8@GA-Fe). Upon

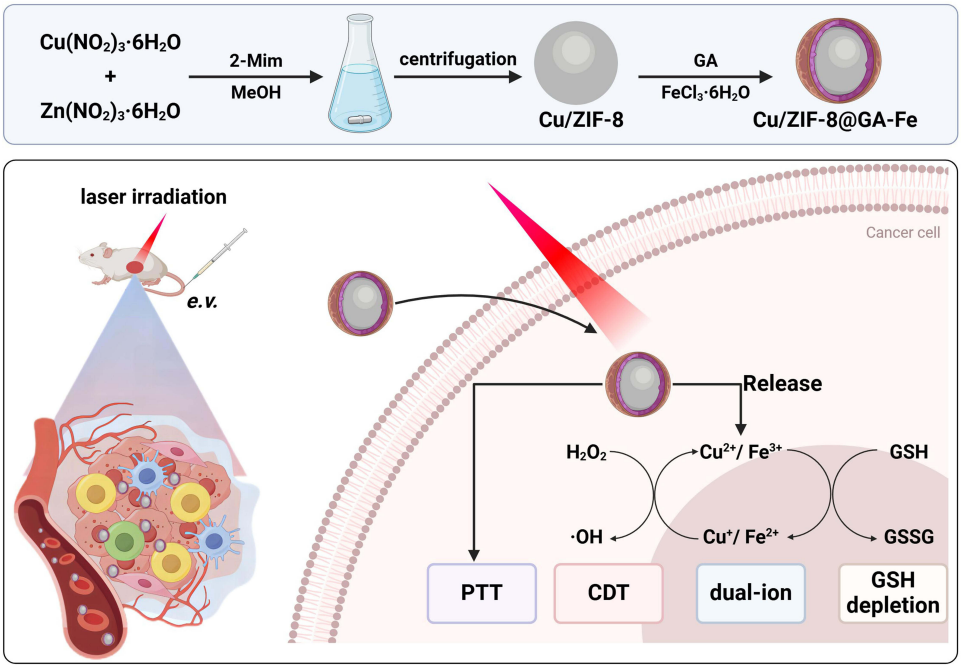

Scheme 1 Schematic of the preparation procedure and mechanism of the Cu/ZIF-8@GA-Fe for combined tumor CDT/PTT Therapy.

internalization by tumor cells, the external GA-Fe coating and Cu/ZIF-8 sequentially dissociate in response to lysosomal acidity, subsequently releasing Fe^{3+} and Cu^{2+}. Notably, the GA-Fe coating imparts photothermal properties to nanocomposites. Under NIR irradiation, the generated heat accelerated the degradation of nanocomposites, thereby enhancing double-ion-mediated ROS generation. At the same time, the released copper and iron ions will synergistically consume a large amount of GSH to weaken the tumor cell's defense against ROS, and at the same time consume a large amount of hydrogen peroxide in the tumor cells to generate hydroxyl radicals. Therefore, through the large amount of ROS production mediated by dual ions, the nano-bomb can effectively inhibit tumor growth in vitro and in vivo.

Materials and Methods

Materials

$Zn(NO_3)_2{\cdot}6H_2O$, $Cu(NO_3)_2{\cdot}6H_2O$, hydrogen peroxide (H_2O_2), 2-methylimidazole, $FeCl_3{\cdot}6H_2O$, L-glutathione reduced (GSH, 98%), methylene blue (MB), 3-(4,5-dimethyl-thiazol-2-yl)-2,5-diphenyltetrazolium bromide (MTT), gallic acid (GA), and 5.5'-Dithiobis-2-nitrobenzoic acid (DTNB) were sourced from Aladdin-Reagent Co. Ltd. The reactive oxygen species detection kit (DCFH-DA), Calcein-AM/propidium iodide (PI) double stain kit, and mitochondrial membrane potential kit with JC-1 were acquired from Beyotime Biotechnology Co., Ltd. Phosphate-buffered saline (1×) (0.0067 M, devoid of calcium and magnesium), Roswell Park Memorial Institute (RPMI) medium 1640, fetal bovine serum (FBS, 10%), and penicillin/streptomycin (1%) were obtained from Keygen Biotech Co., Ltd. (Nanjing, China). Ultrapure water was obtained via a Millipore Autopure system. Unless otherwise stated, all chemicals used were of analytical grade and utilized without additional purification.

Characterization

The morphology of Cu/ZIF-8 and Cu/ZIF-8@GA-Fe was observed using transmission electron microscope (TEM, JEOL 1200EX). The hydrodynamic size and zeta potential of Cu/ZIF-8 and Cu/ZIF-8@GA-Fe were measured by dynamic light scattering (DLS) (Malvern Zetasizer Nano ZS90, UK). The X-ray diffraction (XRD) patterns of Cu/ZIF-8 and Cu/ZIF-8@GA-Fe were recorded with Cu Co radiation (D8ADVANCE, Bruker). X-ray photoelectron spectroscopy (XPS) analysis was conducted using an ESCALAB 250Xi instrument from Thermo Fisher. The absorbance of samples was measured using UV–vis spectroscopy (UV-2550, Shimadzu).

Synthesis of Cu/ZIF-8

Cu/ZIF-8 was prepared according to a reported study.[8] In brief, 2 g of 2-methylimidazole was dissolved into 10 mL of methanol under ultrasonic agitation. After that, 74 mg of $Zn(NO_3)_2{\cdot}6H_2O$ and 20 mg of $Cu(NO_3)_2{\cdot}6H_2O$ were slowly dissolved into 1 mL of methanol under ultrasonic agitation. Subsequently, the resulting solutions were mixed under vigorous stirring (700 rpm) for 48 h, and then the resulting products were harvested by centrifugation and washed with methanol for 3 times. Cu/ZIF-8 was obtained and dried under vacuum at 60°C for 24 hours. Neat ZIF-8 was synthesized using a similar procedure, omitting the addition of $Cu(NO_3)_2{\cdot}6H_2O$.

Synthesis of Cu/ZIF-8@GA-Fe

Cu/ZIF-8@GA-Fe were synthesized by assembling Fe^{3+} and GA on the surface of Cu/ZIF-8 in situ. In brief, 20 mg of Cu/ZIF-8 was dissolved into 20 mL of ultrapure water and processed under ultrasonic agitation. Subsequently, 80 μL of GA (40 mg/mL) and 160 μL of Fe^{3+} (10 mg/mL) were added, followed by immediate vortex mixing for 30 min. The resulting product was separated by centrifugation at 10,000 rpm, washed several times with ultrapure water, and then dried under vacuum at 60°C for 24 hours. The obtained Cu/ZIF-8@GA-Fe was stored at 4 °C until further use.

OH Generation Measurement

Measurement of •OH generation involves utilizing MB as a probe to detect the presence of •OH. In brief, the degradation of MB was evaluated by combining 50 μL of Cu/ZIF-8@GA-Fe (1 mg/mL), 50 μL of H_2O_2 (10 mM), and 2 mL of PBS

containing MB (20 μg/mL). Subsequently, the changes of the absorption peak at 665 nm of the above solutions were detected by UV-visible spectrometer.

GSH Depletion Measurement

For the assessment of GSH depletion induced by Cu/ZIF-8@GA-Fe, spectrophotometric assays based on the reaction of GSH with the specific reagent DTNB were employed. Briefly, the Cu/ZIF-8@GA-Fe solution (1 mg/mL) was cultured with 1 mM GSH. Then, time points were assessed at intervals of 0, 0.5, 1, 2, 3, 4, and 6 hours, and 300 μL of the reaction mixture was added to 1.68 mL of PBS solution (pH 5.5). Subsequently, 20 μL of DTNB solution (0.5 mg/mL in ethanol) was added. GSH depletion was determined using UV-vis spectroscopy by measuring the optical density (OD) at 412 nm.

Photothermal Performance

The photothermal performance of Cu/ZIF-8@GA-Fe was evaluated by monitoring the temperature changes of Cu/ZIF-8@GA-Fe suspensions with concentrations ranging from 0.1 to 1.0 mg/mL under laser irradiation (660 nm, 0.5 W cm^{-2}, 10 min). Subsequently, the temperature of these solutions was measured every 10 seconds using a thermometer. Additionally, the temperature of Cu/ZIF-8@GA-Fe solution with a concentration of 0.5 mg/mL was monitored under different laser irradiation powers (0.1, 0.2, 0.3, 0.4, and 0.5 W cm^{-2}) using the same methodology. Aqueous solution was used as a control.

Cell Experiment

Murine breast cancer 4T1 cells and Human immortalized keratinocytes (HaCaT) cells were both purchased from Wuhan Pricella Biotechnology Co., Ltd. Cells were cultured at 37°C with 5% CO_2 in RPMI medium 1640 supplemented with 10% FBS and 1% penicillin-streptomycin was used for in vitro cell experiments.

In vitro Cytotoxicity

Human immortalized keratinocytes (HaCaT) cells were seeded in 96-well plates and cultured for 24 hours. Subsequently, various concentrations of Cu/ZIF-8@GA-Fe (0, 10, 20, 30, 40, 50, 80, and 100 μg/mL) were added, followed by the incubation for another 24 hours. Afterward, 20 μL per well of MTT solution (5 mg/mL) was introduced and cultured for 4 hours. Finally, 160 μL of dimethyl sulfoxide (DMSO) solution was added to solubilize the formazan crystals formed by metabolically active cells. The cell viability was assessed using a microplate reader by measuring the optical density (OD) at 492 nm.

In vitro Assay for Combination Therapy and Apoptosis Detection

The 4T1 cells were seeded in 96-well plates and cultured for 24 hours. Subsequently, the cells were treated with various treatments including Cu/ZIF-8, GA-Fe, Cu/ZIF-8@GA-Fe, GA-Fe with Laser, and Cu/ZIF-8@GA-Fe with Laser, where the laser power and irradiation time were set at 0.5 W cm^{-2} and 5 minutes, respectively. After incubation for an additional 24 hours, the survival of cells was assessed using the MTT assay.

Live/Dead Cell Staining

4T1 cells were inoculated at a density of 5×10^3 per well and incubated for 12 h in confocal dishes. After that, the cells were co-cultured with various treatments, including Cu/ZIF-8, GA-Fe, Cu/ZIF-8@GA-Fe, GA-Fe with Laser, and Cu/ZIF-8@GA-Fe with Laser, where the laser power and irradiation time were set at 0.5 W cm^{-2} and 5 minutes, respectively. After incubation for an additional 4 hours in 37 °C, the cells were co-incubated with both Calcein-AM and PI for 30 minutes in a humidified atmosphere with 5% CO_2 at 37°C according to the manufacturer's instructions. Afterward, the cells were washed with PBS for 3 times and observed through a confocal laser scanning microscope (CLSM).

ROS Staining

Dichlorofluorescein diacetate (DCFH-DA) is commonly utilized for detecting intracellular ROS. Initially, 4T1 cells were seeded (1×10^5 cells per well) in 6-well plates and incubated for another 24 hours. Subsequently, the cells in the 6-well

plates were subjected to various treatments, including Cu/ZIF-8, GA-Fe, Cu/ZIF-8@GA-Fe, GA-Fe with Laser, and Cu/ZIF-8@GA-Fe with Laser, where the laser power and irradiation time were set at 0.5 W cm^{-2} and 5 minutes, respectively. After incubation for an additional 4 hours, the cells were stained with DCFH-DA for 10 minutes to visualize ROS. Fluorescence detection of DCF was performed using an excitation with the wavelength of 485 nm and an emission with the wavelength of 525 nm.

Evaluation of Mitochondrial Membrane Potential

4T1 cells were cultured in 6-well plates under various treatment conditions. Subsequently, the medium from each well was removed, and 1 mL of fresh medium containing JC-1 staining solution was added. Following an incubation for 20 minutes, the supernatant was removed, and the cells were washed for 2 times using JC-1 staining buffer. Finally, 2 mL of fresh medium was introduced to each well, and the cells were observed using a fluorescence microscope.

In vivo Experiment

Balb/c female mice (5–6 weeks) were purchased from Ling Chang Biotechnology Co., Ltd. (Shanghai China). All experimental procedures were approved by the Ethics Committee of the Second Affiliated Hospital, School of Medicine, Zhejiang University, and conducted according to the Institutional Animal Care and Use Committee (IACUC) guidelines. 4T1 tumor models were established by subcutaneously injecting approximately 1×10^6 4T1 cells into female Balb/c mice. After the volume of the tumor reached 80–100 mm^3, the mice were randomly divided into six groups (n=6 per group), including control group receiving intratumoral injection with PBS, and treatment groups receiving intratumoral injection with Cu/ZIF-8, GA-Fe, Cu/ZIF-8@GA-Fe, GA-Fe with laser irradiation (0.5 W cm^2 for 5 minutes), and Cu/ZIF-8@GA-Fe with laser irradiation (0.5 W cm^2 for 5 minutes). The tumor size was measured and calculated as volume (width^2 × length × 0.5). After 21 days post-injection, the harvested tumor tissue was fixed with 4% paraformaldehyde, processed into paraffin sections, and stained with hematoxylin and eosin (H&E) according to the manufacturer's instructions.

Statistical Analyses

For each experiment, we performed at least three replications to ensure the stability and reliability of the results. The statistical significance of differences between groups was determined by using one-way ANOVA followed by Tukey post-hoc analysis. Significance was established by a value of $p < 0.05$. Statistical analysis was performed with Origin.

Results and Discussion

Preparation and Characterization of Cu/ZIF-8@GA-Fe

The preparing procedure of Cu/ZIF-8@GA-Fe was shown in Scheme 1, where it could be seen that Cu/ZIF-8@GA-Fe were prepared by doping copper ions into ZIF-8 and in situ assembling Fe^{3+} and GA on its surface. Initially, Cu/ZIF-8 nanoparticles were synthesized through a simple ion-doping method.[8] Data from TEM image suggested that the obtained Cu/ZIF-8 possessed a dodecahedral structure with a diameter of around ~100 nm (Figure 1a). In addition, the TEM enlarged image shows that Cu/ZIF-8 has a better dodecahedral structure (Figure S1), which demonstrated that the doping of Cu ions did not disrupt the main structure of ZIF-8. To enhance the efficiency of ROS generation for CDT and improve material dispersion, we coated GA-Fe onto the surface of Cu/ZIF-8. As shown in Figure 1b, the presence of a polymer layer on the Cu/ZIF-8 surface in the TEM confirms the successful synthesis of Cu/ZIF-8@GA-Fe. Further validation of the successful synthesis was achieved through XRD analysis of Cu/ZIF-8 and Cu/ZIF-8@GA-Fe, as illustrated in Figure 1c. The XRD patterns of as-prepared Cu/ZIF-8 and Cu/ZIF-8@GA-Fe closely resembled those of simulated ZIF-8, which could be attributed to the fact that the addition of copper ions and GA-Fe barely disrupt the crystal structure of ZIF-8. Additionally, the effective in situ self-assembly of GA and Fe^{3+} on the surface of Cu/ZIF-8@GA-Fe was confirmed by DLS and zeta potential analysis (Figure 1d and e). The increase in the hydrodynamic particle size of Cu/ZIF-8@GA-Fe to 190 nm compared to Cu/ZIF-8 and the decrease in the surface potential from +24 mV to −27 mV were attributed to the successful coating of GA-Fe on the Cu/ZIF-8 surface. Furthermore, the color change of Cu/ZIF-8 from brown to black after coating with GA-Fe was visually observed (Figure S2). Notably, compared to Cu/ZIF-8, Cu/ZIF-8@GA-Fe exhibited strong absorption across the visible and near-infrared (NIR) regions, with a characteristic absorption

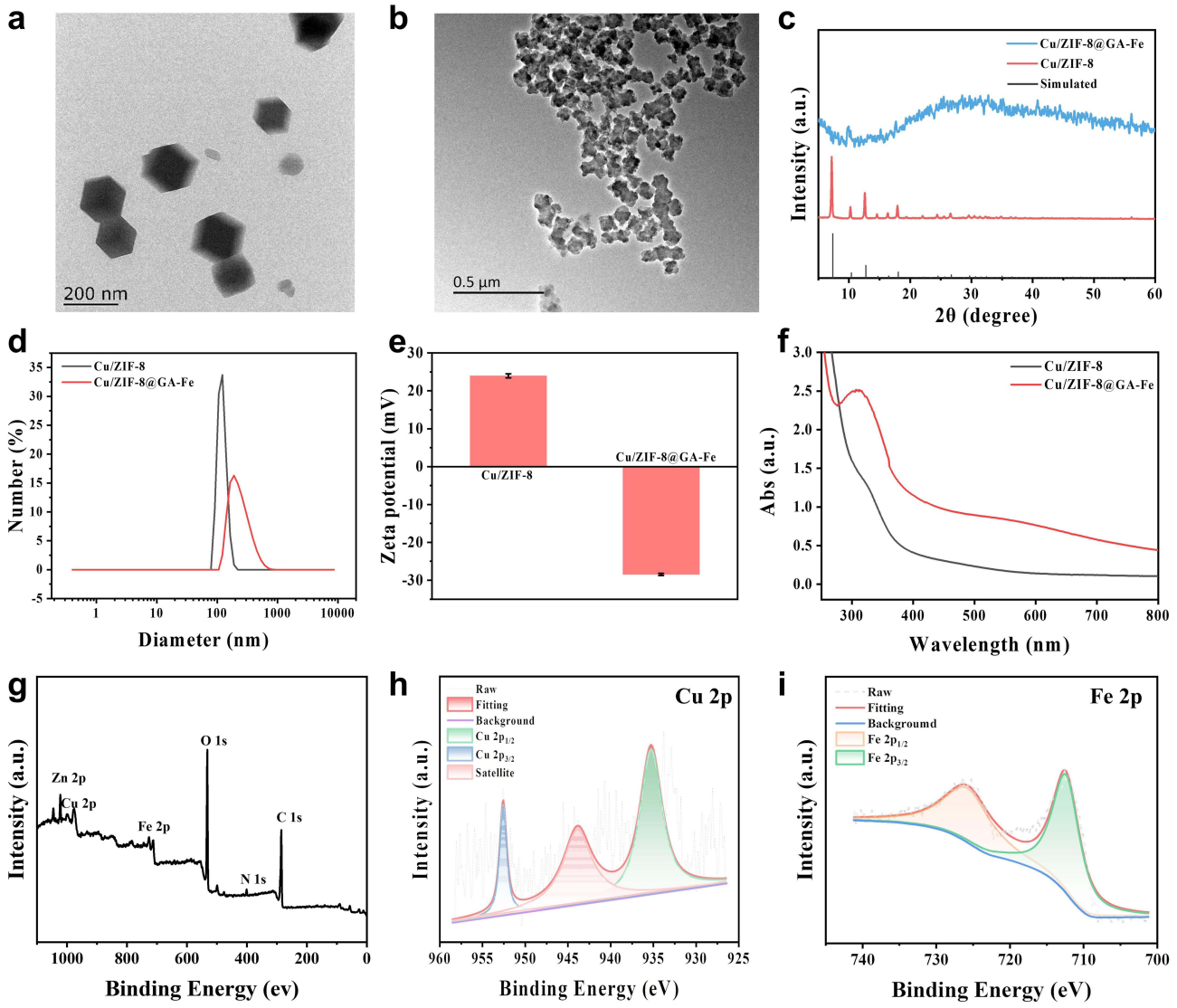

Figure 1 Characterization of as-prepared Cu/ZIF-8@GA-Fe. Typical TEM image of (**a**) Cu/ZIF-8 and (**b**) Cu/ZIF-8@GA-Fe, respectively. (**c**) XRD patterns, (**d**) DLS, (**e**) Zeta potential, (**f**) UV-vis spectrum of the as-prepared Cu/ZIF-8 and Cu/ZIF-8@GA-Fe, respectively. (**g**) XPS survey of Cu/ZIF-8@GA-Fe. (**h**) Cu 2p spectrum of Cu/ZIF-8@GA-Fe. (**i**) Fe 2p spectrum of Cu/ZIF-8@GA-Fe.

peak at 600 nm possibly attributed to the d-d electronic transition of the GA-Fe complex (Figure 1f). The chemical composition and ion valence of Cu/ZIF-8@GA-Fe were further elucidated using XPS. And further analysis revealed the presence of Cu, Zn, Fe, C, N, and O elements in Cu/ZIF-8@GA-Fe (Figure 1g). The Cu 2p spectrum of Cu/ZIF-8@GA-Fe displayed peaks at 935.2 eV and 952.5 eV corresponding to Cu $2p_{3/2}$ and Cu $2p_{1/2}$ of Cu^{2+} (Figure 1h). Subsequently, the Fe 2p spectrum (Figure 1i) exhibited strong peaks at approximately 711.28 eV and 724.97 eV, indicative of Fe $2p_{3/2}$ and Fe $2p_{1/2}$, respectively, indicating the presence of Fe^{3+}. The above results indicate that surface modification of GA-Fe successfully doped Cu ions in the ZIF-8 structure.

The ROS Generation, H_2O_2 and GSH Consumption and Photothermal Properties of Cu/ZIF-8@GA-Fe

The generation of •OH from Cu/ZIF-8@GA-Fe was assessed using MB as an indicator. Initially, we investigated the capacity of Cu/ZIF-8@GA-Fe to produce ROS at physiological pH (pH=7.4). As demonstrated in Figure 2a, negligible changes were observed in the absorption peak of MB, indicating minimal ROS generation by Cu/ZIF-8@GA-Fe under

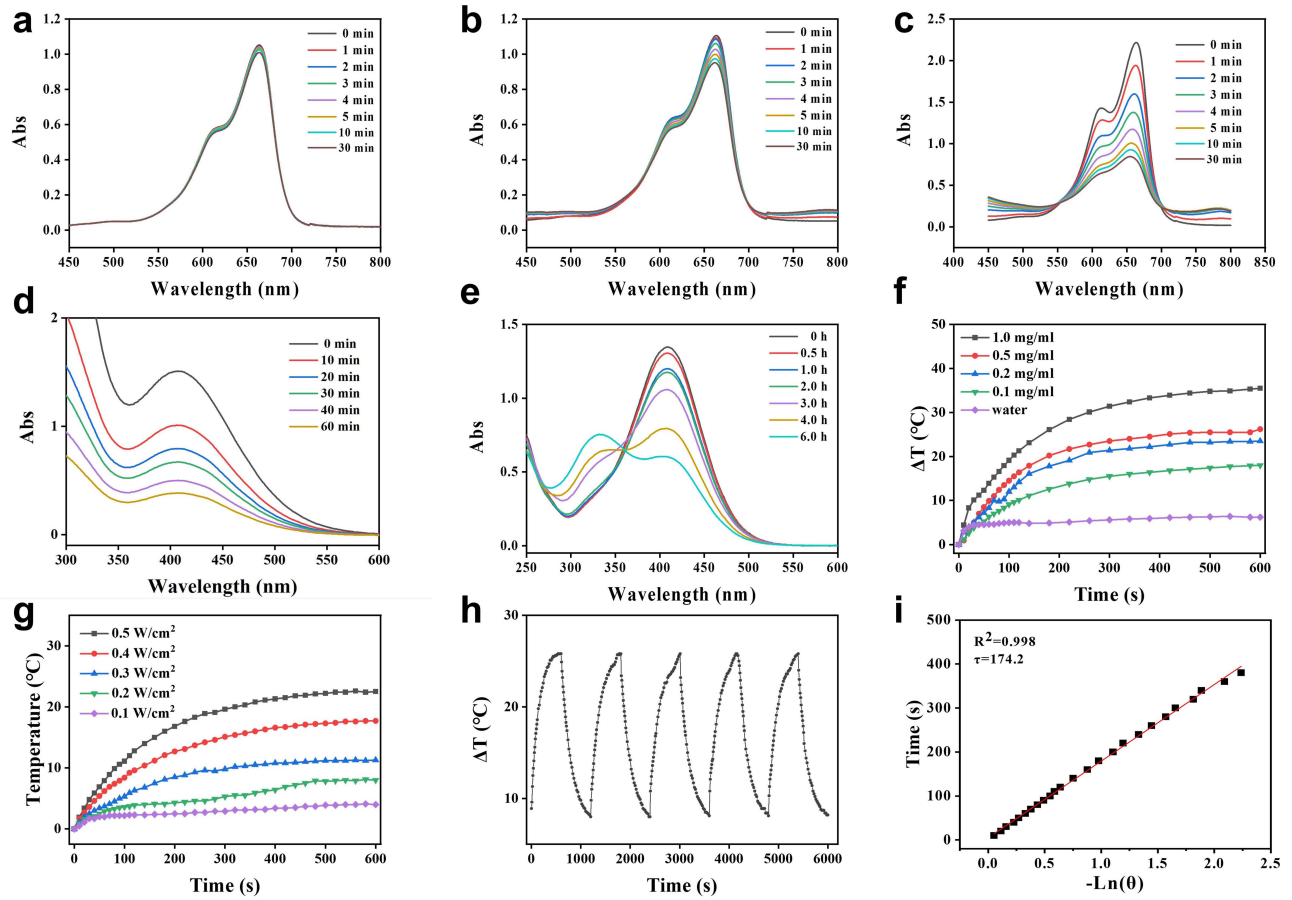

Figure 2 MB degradation of Cu/ZIF8@GA-Fe in (**a**) physiological environment (pH 7.4), (**b**) weakly acidic environment (pH 6.5), (**c**) pH 6.5 with laser irradiation. (**d**) H_2O_2 degradation of Cu/ZIF8@GA-Fe. (**e**) GSH depletion of Cu/ZIF8@GA-Fe in pH 6.5. (**f**) Temperature changes of Cu/ZIF8@GA-Fe with various concentrations upon 660 nm laser irradiation treatment (1 W cm^{-2}). (**g**) Heating curves of Cu/ZIF8@GA-Fe (0.5 mg/mL) under 660 nm laser irradiation treatment with various power densities ranging from 0.1 to 0.5 W cm^{-2} for 10 min. (**h**) Recycling heating curves of Cu/ZIF8@GA-Fe (0.5 mg/mL) with laser (0.5 W cm^{-2}). (**i**) Corresponding cooling time constant (τ_s) calculation.

normal physiological conditions, resulting in minimal and specific damage to normal tissues. However, in a weakly acidic environment (pH=6.5), Cu/ZIF-8@GA-Fe exhibited a remarkable decrease in the absorption peak of MB within 30 minutes (Figure 2b), suggesting its robust acid-responsive and ROS-generating properties. Remarkably, when MB was subjected to a weakly acidic environment combined with laser irradiation, a substantial reduction in the characteristic absorption peaks of MB was observed (Figure 2c). This observation indicated that the photothermal effect significantly facilitated the Fenton/Fenton-like reactions involving copper and iron ions, leading to rapid ROS generation within 30 minutes. Previous studies were focused on the heat generated by PTT to promote single ion-mediated ROS production, whereas the present study innovatively used heat to promote two ion-mediated Fenton reactions to generate more ROS, which would greatly enhance the killing of tumor cells.

To further validate the underlying catalytic mechanism of Cu/ZIF-8@GA-Fe involving the decomposition of hydrogen peroxide via Fenton and Fenton-like reactions, we employed titanium sulfate-based colorimetry to confirm its hydrogen peroxide consumption capability. As illustrated in Figure 2d, the absorption peak at 412 nm exhibited a notable decrease of approximately 65% within 60 minutes, underscoring the excellent hydrogen peroxide consumption ability of Cu/ZIF-8@GA-Fe, which was attributed to the occurrence of the double-ion-mediated Fenton/Fenton-like reaction. Moreover, DTNB was employed to evaluate the utilization of glutathione (GSH), given its susceptibility to reduction by GSH, resulting in a yellow product characterized by an absorption peak at 412 nm. As shown in Figure 2e, a sharp decline in absorbance at 412 nm was observed over time, with the absorption value decreasing by approximately 40% within 6 hours. This indicated the ability of Cu^{2+} and Fe^{3+} ions released from Cu/ZIF-8@GA-Fe in acidic environments

to rapidly deplete GSH, which would greatly disrupt the resistance of overexpressed GSH to ROS in tumor cells and enhance the therapeutic efficacy of CDT. Moreover, we investigated the photothermal conversion properties of Cu/ZIF8@GA-Fe. As depicted in Figure 2f, the temperature of Cu/ZIF8@GA-Fe increased at low concentrations, with its photothermal effect being influenced by concentration changes. At a concentration of 1 mg/mL, the temperature elevation value reached approximately 35 degrees Celsius, which was adequate for photothermal therapy (PTT). On the contrary, the temperature fluctuation of the aqueous solution under the same laser irradiation condition was small, which further indicated that the temperature increase of the Cu/ZIF8@GA-Fe aqueous solution originated from the excellent photothermal conversion property of GA-Fe. The photothermal conversion efficiency of Cu/ZIF8@GA-Fe was predominantly influenced by laser power density (Figure 2g), with noticeable enhancement in temperature observed with increasing intensity of the laser power. Notably, following sustained 660 nm laser irradiation for 5 cycles, the temperature changes exhibited no detectable fluctuation, indicative of the excellent photothermal stability of Cu/ZIF8@GA-Fe (Figure 2h). Finally, the calculated photothermal conversion efficiency (PCE) at 808 nm was determined to be 34.6% (Figure 2i), the value of which was high than that of the reported photothermal agents (MnO_2 sheets, 21.4%; Cu_9S_5, 25.7%).

In vitro Assays

Biocompatibility of nanomaterials is paramount for their successful integration and safe use within biological systems.[32] In order to verify the non-specificity of Cu/ZIF8@GA-Fe on normal cells, considering the existing conditions in the laboratory, we chose Human immortal keratinocyte line (HaCaT) as a model cell for normal cells. Hence, the biocompatibility assay of Cu/ZIF8@GA-Fe was initially conducted by assessing the viability of HaCaT cells cultured with Cu/ZIF8@GA-Fe using MTT assay. As illustrated in Figure 3a, the viability of HaCaT cells exceeded 80% even at Cu/ZIF8@GA-Fe concentrations as high as 200 ppm, indicating excellent compatibility of Cu/ZIF8@GA-Fe and did not

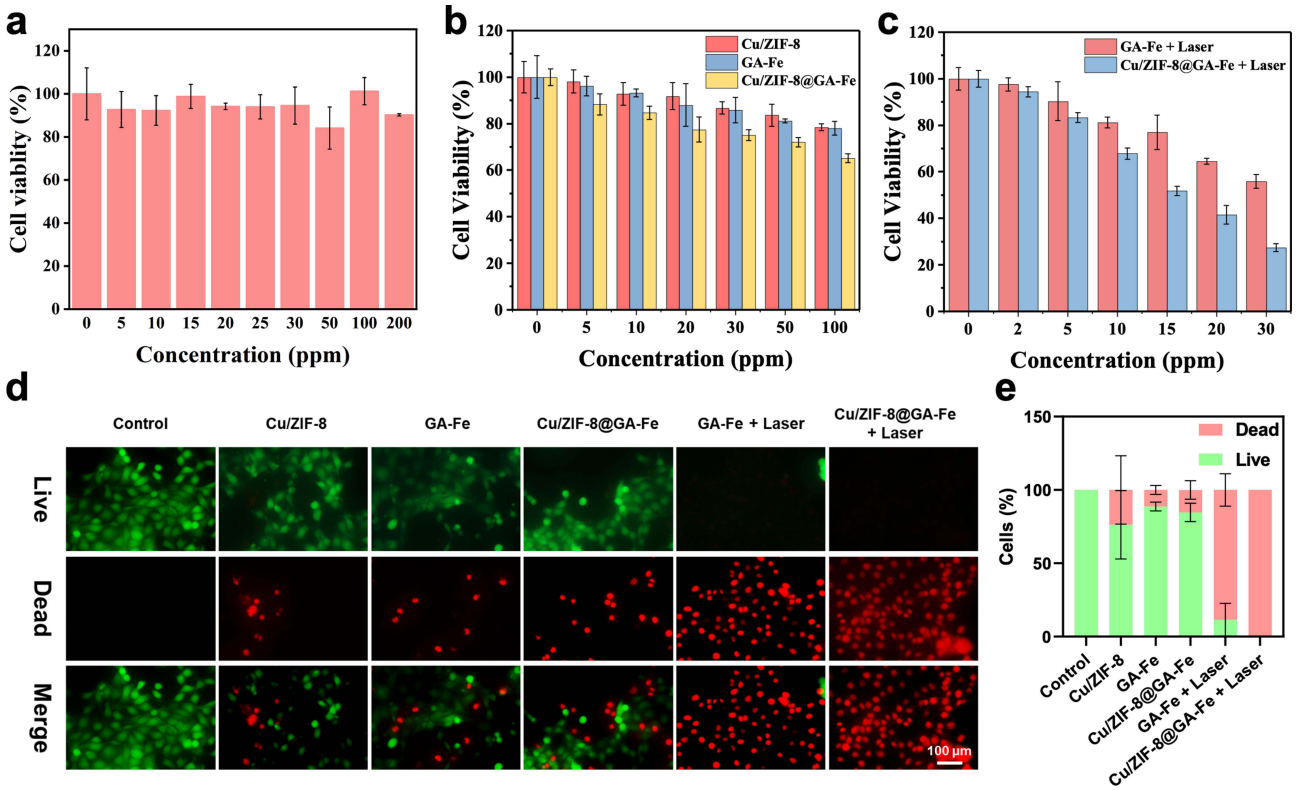

Figure 3 (**a**) Viability of HaCaT cells after incubation with Cu/ZIF-8@GA-Fe at various concentrations. (**b**) Cell viability of 4T1 cells cultured with various treatments. (**c**) Cell viability of 4T1 cells incubated with various treatments under laser irradiation. (**d**) Calcein-AM/PI double staining of 4T1 cells after various treatments. (**e**) Quantitative fluorescence analysis of live-dead staining.

cause damage to normal cells or tissues. Subsequently, we investigated the toxicity of various components (Cu/ZIF-8, GA-Fe, Cu/ZIF8@GA-Fe) on 4T1 cells in the absence of laser radiation. Surprisingly, as depicted in Figure 3b, Cu/ZIF-8@GA-Fe exhibited higher dark toxicity compared to Cu/ZIF-8 and GA-Fe alone, suggesting that dual-ion-based CDT possesses greater inhibitory effects on 4T1 cell activity. Based on these findings, we further explored the inhibitory effects of GA-Fe and Cu/ZIF-8@GA-Fe on the viability of 4T1 cells under laser radiation. As depicted in Figure 3c, the inhibition of 4T1 cell viability by Cu/ZIF-8@GA-Fe was significantly enhanced following laser irradiation, outperforming the effect observed in the absence of laser radiation (Figure 3b). This enhancement might be attributed to the dual action of PTT, which not only inhibits 4T1 cell viability but also augments CDT. Additionally, GA-Fe exhibited a similar trend under light exposure. Calcein-AM/PI double staining method was used to further observe the tumor cell killing property of Cu/ZIF-8@GA-Fe. As shown in the live-dead staining images of Figure 3d and the results of its quantitative fluorescence analysis (Figure 3e), the control, Cu/ZIF-8, and GA-Fe groups induced minimal cell death, whereas the introduction of dual ions in the Cu/ZIF-8@GA-Fe group led to a notable increase in tumor cell death. Furthermore, due to the enhanced generation of hydroxyl radicals (•OH) and photothermal effects, substantial increase of the red signal could be observed in the GA-Fe + Laser and Cu/ZIF-8@GA-Fe + Laser groups. These results indicated that the combination of PTT and CDT with Cu/ZIF-8@GA-Fe had high toxicity to tumor cells.

To further confirm the generation of •OH through Fenton and Fenton-like reactions at the cellular level by Cu/ZIF-8@GA-Fe, we stained 4T1 cells subjected to various treatments with DCFH-DA. As illustrated in Figure 4a and b, slight fluorescence in the Cu/ZIF-8 and GA-Fe groups could be observed compared to the control group without green

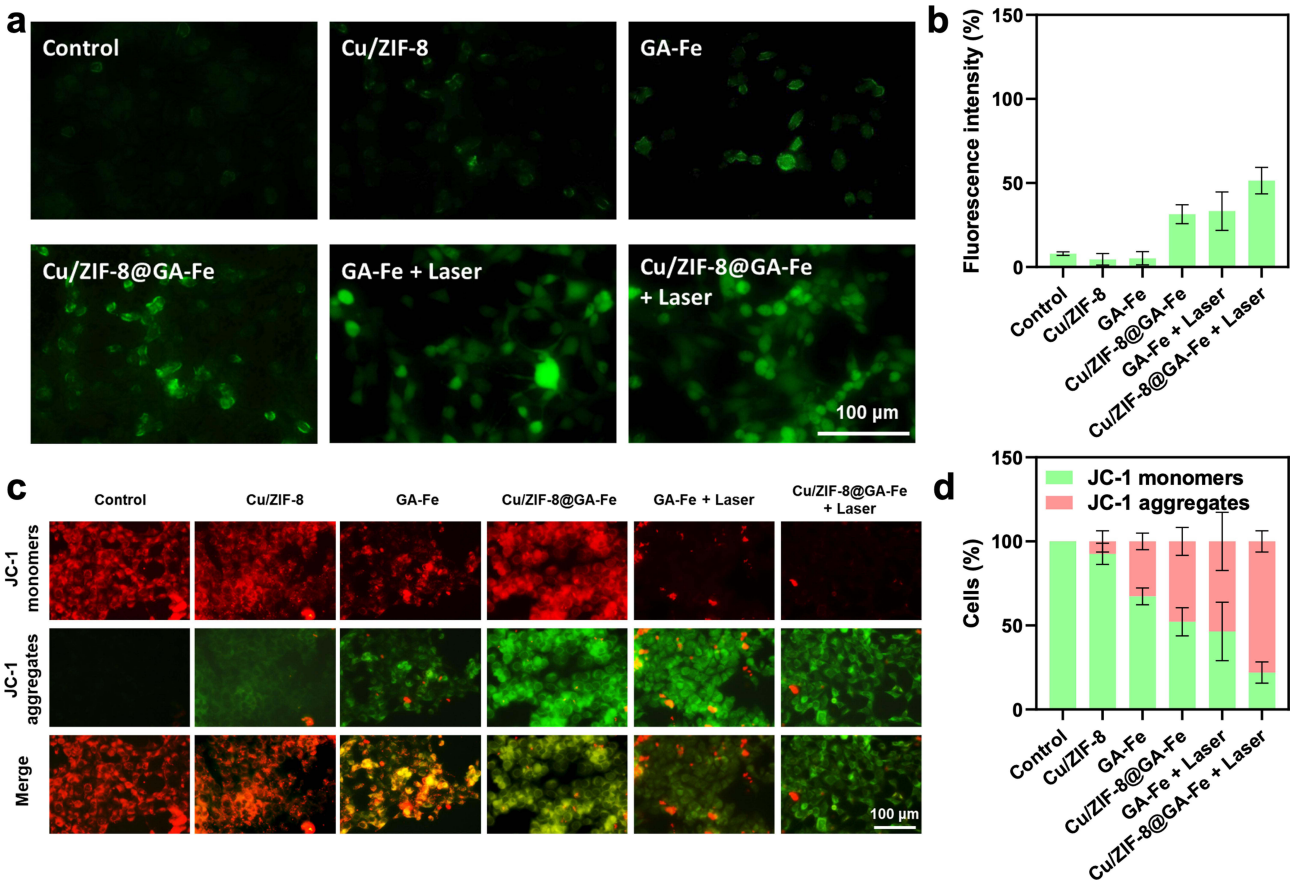

Figure 4 (**a**) ROS staining (**b**) and corresponding fluorescence quantitative analysis intensity results (**c**) JC-1 staining (**d**) and corresponding fluorescence quantitative analysis intensity results of 4T1 cells under different treatments.

fluorescence, which could be attributed to the insufficient H_2O_2 at the cellular level for the Fenton and Fenton-like reactions. Upon treatment with Cu/ZIF-8@GA-Fe, the generation of •OH increased and further enhanced under laser irradiation, which could be attributed to the enhanced Fenton-like reaction induced by photothermal effects. Additionally, the GA-Fe + Laser group also promote the generation of •OH, indicating that photothermal effects could facilitate the Fenton reaction.

It has been reported that ROS and heat can induce mitochondrial dysfunction and cellular damage.[33] Changes in mitochondrial membrane potential were assessed using the fluorescent probe JC-1. As depicted in Figure 4c and d, in comparison with the control's red fluorescence, 4T1 cells treated with Cu/ZIF-8 and GA-Fe displayed overlapped red and green fluorescence, accompanied by a reduction in red fluorescence intensity and the emergence of orange signals, indicating mitochondrial perturbation due to •OH. Remarkably, cells treated with Cu/ZIF-8@GA-Fe, GA-Fe + Laser, and Cu/ZIF-8@GA-Fe + Laser exhibited notable increases in green fluorescence, suggesting that the combined therapy could profoundly impair mitochondrial function, thereby leading to cellular death. Cu/ZIF-8@GA-Fe can promote the generation of a large amount of ROS by the dual-ion-mediated Fenton/Fenton-like reaction through the photothermal effect at the cellular level, leading to cellular mitochondrial membrane potential damage, inducing apoptosis, and then killing tumor cells.

In vivo Antitumor Effect of Cu/ZIF-8@GA-Fe

The promising performance of Cu/ZIF-8@GA-Fe in vitro prompted further investigation into its in vivo efficacy, the process of which was schematically shown in Figure 5a. 4T1 tumor-bearing Balb/c mice were used as tumor model for in vivo assessment of antitumor performance of Cu/ZIF-8@GA-Fe in the present of laser radiation. The mice were randomly divided into six groups, including control, Cu/ZIF-8, GA-Fe, GA-Fe + Laser, Cu/ZIF-8@GA-Fe, and Cu/ZIF-8@GA-Fe + Laser treatments, respectively. Hemolysis tests were conducted prior to in vivo investigations to assess the safety and biocompatibility of Cu/ZIF-8@GA-Fe as an intravenous drug delivery formulation. The hemolysis rates of Cu/ZIF-8@GA-Fe at doses between 100 and 500 μg/mL were lower than 5% threshold, suggesting that Cu/ZIF-8@GA-Fe had acceptable blood biocompatibility (Figure 5b). To further assess the systemic toxicity of Cu/ZIF-8@GA-Fe towards mice, data from the body weight of mice throughout the 21 days of intravenous injection demonstrated that the bodyweight of mice exhibited slight changes, indicating that all the investigated treatment barely had negative effects towards mice (Figure 5c). We further measured the volumes of tumors to assess their antitumor performance in vivo, As illustrated in Figure 5d, Cu/ZIF-8 and GA-Fe groups exhibited low therapeutic efficacy due to the lower ROS yield associated with single-ion-based CDT. In Cu/ZIF-8@GA-Fe-treated mice, the inhibition of tumor growth may be due to the combined effect of GSH depletion and bionic-mediated CDT production of more ROS. Moreover, although GA-Fe + Laser also demonstrated a better inhibitory effect, Cu/ZIF-8@GA-Fe + Laser exhibited a more dramatic tumor inhibitory effect due to the significant enhancement of dual-ion-based CDT by photothermal effects, which was consistent with the results of Figure 5e.

The systemic toxicity of combined tumor CDT/PTT therapy strategies was further investigated through histological examinations. As demonstrated in Figure S3, no visible inflammatory response and pathological features in major organs, including heart, liver, spleen, lung and kidney of mice could be observed at the tissue level in all investigated groups, implying scarcely any systemic toxicity towards mice during the combined tumor CDT/PTT treatment. Moreover, the H&E staining of tumors in various investigated groups (Figure 5f) showed that Cu/ZIF-8@GA-Fe + Laser group exhibited the most severe damage to the tumor tissues. Taken together, these in vivo results confirmed that the Cu/ZIF-8@GA-Fe + Laser group possessed good biocompatibility and simultaneously inhibited tumor growth. In the future, Cu/ZIF-8@GA-Fe could be used in combination with other treatments (eg, chemotherapy, radiotherapy, immunotherapy) to achieve a more comprehensive therapeutic efficacy and reduce the possibility of tumor recurrence.

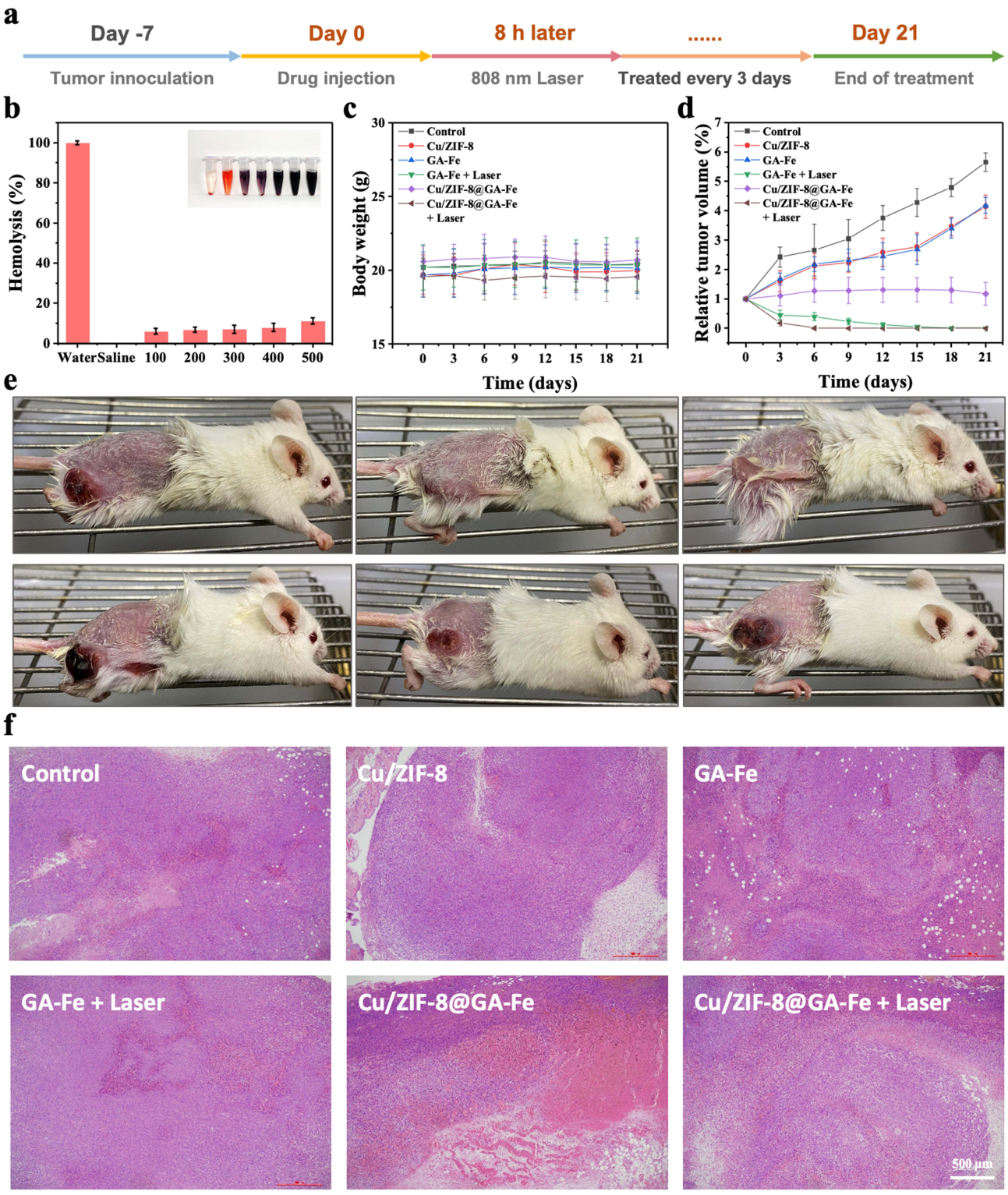

Figure 5 (**a**) Schematic diagram of animal experiment process. (**b**) Hemolytic test results. (**c**) Results of body weight and (**d**) Relative tumor volume recordings for each group of mice during the treatment period. (**e**) Photographs of mice with different treatment at the time of the first treatment. (**f**) H&E staining of tumor tissue from each group of mice. Scale bar: 500 μm.

Conclusions

In conclusion, a dual-ion based ROS nano-bomb for combined tumor therapy was successfully developed. The incorporation of copper and iron ions in Cu/ZIF-8@GA-Fe not only facilitated the depletion of GSH but also promoted

the generation of ROS, effectively inducing apoptosis in murine breast tumor cells. In addition, Cu/ ZIF-8@GA-Fe also has good photothermal conversion and photothermal stability. Therefore, the induced heat amplifies these chemical processes under laser irradiation, resulting in enhanced tumor cell death. In vitro experiments have shown that at a lower concentration of cells, Cu/ZIF-8@GA-Fe can have a strong inhibitory effect on tumor growth. In vivo experiments have shown that Cu/ZIF-8@GA-Fe being able to effectively ablate tumor tissue does not cause physiological toxicity. Cu/ZIF-8@GA-Fe, as a new type of ROS nano-bomb, has broad application prospects in tumor treatment and is expected to bring safer, more effective, and personalized treatment options for patients with malignancies. With the advancement of clinical trials and the continuous maturity of related technologies, we look forward to it benefiting a large number of cancer patients as soon as possible.

Acknowledgments

This work was supported by the Natural Science Foundation of Zhejiang Province (LQ23H070003), Science program of Jiangsu Province Administration for Market Regulation (KJ2024010).

Author Contributions

JK, MW, and JL: original draft writing; YX, HH: Data curation; JG, TP: Methodology and Formal analysis; JL, ZL, and LJ: responses to editor and reviewers; ZL, LJ: Supervision. All authors made a significant contribution to the work, whether that is in the concept generation, study design, execution, acquisition of data, analysis and interpretation, or any other areas. We took part in drafting, revising or critically reviewing the article; gave final approval of the version to be published; have agreed with the journal in which the article was submitted; and agree to be accountable for all aspects of the work.

Disclosure

The authors declare no competing interest in this work.

References

1. Cheung EC, Vousden KH. The role of ROS in tumour development and progression. *Nat Rev Cancer*. 2022;22(5):280–297. doi:10.1038/s41568-021-00435-0
2. Wu H, Yuan Y, Kang S, et al. Autophagy inhibitor-loaded mesoporous AgNPs@SiO2 nanoplatform for synergistically enhanced glioma radiotherapy. *Sci China Mater*. 2023;66(7):2902–2912. doi:10.1007/s40843-022-2395-y
3. Wang Y, Lu Z, Liu B, et al. Antitumor effects of carrier-free functionalized lignin materials on human hepatocellular carcinoma (HepG2) Cells. *ACS Nano*. 2024;18(5):4329–4342. doi:10.1021/acsnano.3c09924
4. Sun J, Fan Y, Ye W, et al. Near-infrared light triggered photodynamic and nitric oxide synergistic antibacterial nanocomposite membrane. *Chem Eng J*. 2021;417:128049. doi:10.1016/j.cej.2020.128049
5. Yu Y, Wu S, Zhang L, et al. Cationization to boost both type I and type II ROS generation for photodynamic therapy. *Biomaterials*. 2022;280:121255. doi:10.1016/j.biomaterials.2021.121255
6. Dong Y, Dong S, Liu B, et al. 2D Piezoelectric Bi(2) MoO(6) Nanoribbons for GSH-enhanced sonodynamic therapy. *Adv Mater*. 2021;33(51):e2106838. doi:10.1002/adma.202106838
7. Yin YF, Jiang XW, Sun LP, et al. Continuous inertial cavitation evokes massive ROS for reinforcing sonodynamic therapy and immunogenic cell death against breast carcinoma. *Nano Today*. 2021;36:101009. doi:10.1016/j.nantod.2020.101009
8. Wang L, Xu YT, Liu C, et al. Copper-doped MOF-based nanocomposite for GSH depleted chemo/photothermal/chemodynamic combination therapy. *Chem Eng J*. 2022;438:135567. doi:10.1016/j.cej.2022.135567
9. Wang S, Yu G, Wang Z, et al. Enhanced antitumor efficacy by a cascade of reactive oxygen species generation and drug release. *Angew Chem*. 2019;58(41):14758–14763. doi:10.1002/anie.201908997
10. Wang XW, Zhong XY, Liu Z, Cheng L. Recent progress of chemodynamic therapy-induced combination cancer therapy. *Nano Today*. 2020;35:100946. doi:10.1016/j.nantod.2020.100946
11. Zhong X, Wang X, Cheng L, et al. GSH-Depleted PtCu3 nanocages for chemodynamic- enhanced sonodynamic cancer therapy. *Adv Funct Mater*. 2019;30(4):1. doi:10.1002/adfm.201907954
12. Wu H, Lin J, Liu P, et al. Reactive oxygen species acts as executor in radiation enhancement and autophagy inducing by AgNPs. *Biomaterials*. 2016;101:1–9. doi:10.1016/j.biomaterials.2016.05.031
13. Tian H, Yan J, Zhang W, et al. Cu-GA-coordination polymer nanozymes with triple enzymatic activity for wound disinfection and accelerated wound healing. *Acta Biomater*. 2023;167:449–462. doi:10.1016/j.actbio.2023.05.048
14. Wang X, Shi Q, Zha Z, et al. Copper single-atom catalysts with photothermal performance and enhanced nanozyme activity for bacteria-infected wound therapy. *Bioact Mater*. 2021;6(12):4389–4401. doi:10.1016/j.bioactmat.2021.04.024
15. Wang X, Zhong X, Lei H, et al. Hollow Cu2Se Nanozymes for Tumor Photothermal-Catalytic Therapy. *Chem Mater*. 2019;31(16):6174–6186. doi:10.1021/acs.chemmater.9b01958

16. Wang X, Zhong X, Zha Z, et al. Biodegradable CoS2 nanoclusters for photothermal-enhanced chemodynamic therapy. *Appl Mater Today*. 2020;18:100464. doi:10.1016/j.apmt.2019.100464
17. Altaf MA, Shahid R, Ren MX, et al. Melatonin improves drought stress tolerance of tomato by modulating plant growth, root architecture, photosynthesis, and antioxidant defense system. *Antioxidants*. 2022;11(2):1. doi:10.3390/antiox11020309
18. Niu B, Liao K, Zhou Y, et al. Application of glutathione depletion in cancer therapy: enhanced ROS-based therapy, ferroptosis, and chemotherapy. *Biomaterials*. 2021;277:121110. doi:10.1016/j.biomaterials.2021.121110
19. Guo Q, Yin M, Fan J, et al. Peroxidase-mimicking TA-VOx nanobranches for enhanced photothermal/chemodynamic therapy of glioma by inhibiting the expression of HSP60. *Mater Des*. 2022;224:111366. doi:10.1016/j.matdes.2022.111366
20. Shen Y, Nie C, Pan T, et al. A multifunctional cascade nanoreactor based on Fe-driven carbon nanozymes for synergistic photothermal/chemodynamic antibacterial therapy. *Acta Biomater*. 2023;168:580–592. doi:10.1016/j.actbio.2023.07.006
21. Siddique S, Chow JCL. Application of nanomaterials in biomedical imaging and cancer therapy. *Nanomaterials*. 2020;10(9):1700. doi:10.3390/nano10091700
22. Wang X, Zhao L, Wang C, et al. Potent nanoreactor-mediated ferroptosis-based strategy for the reversal of cancer chemoresistance to Sorafenib. *Acta Biomater*. 2023;159:237–246. doi:10.1016/j.actbio.2023.01.053
23. Guo N, Xia Y, Duan Y, et al. Self-enhanced photothermal-chemodynamic antibacterial agents for synergistic anti-infective therapy. *Chin Chem Lett*. 2023;34(2):107542. doi:10.1016/j.cclet.2022.05.056
24. Koo S, Park OK, Kim J, et al. Enhanced chemodynamic therapy by Cu-Fe peroxide nanoparticles: tumor microenvironment-mediated synergistic Fenton reaction. *ACS nano*. 2022;16(2):2535–2545. doi:10.1021/acsnano.1c09171
25. Liu D, Liu M, Wan Y, et al. Remodeling endogenous H2S microenvironment in colon cancer to enhance chemodynamic therapy. *Chem Eng J*. 2021;422:130098. doi:10.1016/j.cej.2021.130098
26. Liu Y, Guo Z, Li F, et al. Multifunctional magnetic copper ferrite nanoparticles as Fenton-like reaction and near-infrared photothermal agents for synergetic antibacterial therapy. *ACS Appl Mater Interfaces*. 2019;11(35):31649–31660. doi:10.1021/acsami.9b10096
27. Feng SP, Lu JY, Wang KL, et al. Advances in smart mesoporous carbon nanoplatforms for photothermal-enhanced synergistic cancer therapy. *Chem Eng J*. 2022;435:134886. doi:10.1016/j.cej.2022.134886
28. Zhang L, Liu Y, Huang H, et al. Multifunctional nanotheranostics for near infrared optical imaging-guided treatment of brain tumors. *Adv. Drug Delivery Rev*. 2022;190:114536. doi:10.1016/j.addr.2022.114536
29. Wang P, Sun W, Wang Q, et al. Iodine-labeled au nanorods with high radiochemical stability for imaging-guided radiotherapy and photothermal therapy. *ACS Appl Nano Mater*. 2019;2(3):1374–1381. doi:10.1021/acsanm.8b02229
30. Hu K, Xie L, Zhang Y, et al. Marriage of black phosphorus and Cu(2+) as effective photothermal agents for PET-guided combination cancer therapy. *Nat Commun*. 2020;11(1):2778. doi:10.1038/s41467-020-16513-0
31. Zhang Q, Guo Q, Chen Q, Zhao X, Pennycook SJ, Chen H. Highly efficient 2D NIR-II photothermal agent with Fenton catalytic activity for cancer synergistic photothermal-chemodynamic therapy. *Adv Sci*. 2020;7(7):1902576. doi:10.1002/advs.201902576
32. Zheng L, Zhuang Z, Li Y, et al. Bone targeting antioxidative nano-iron oxide for treating postmenopausal osteoporosis. *Bioact Mater*. 2022;14:250–261. doi:10.1016/j.bioactmat.2021.11.012
33. Guo C, Sun L, Chen X, Zhang D. Oxidative stress, mitochondrial damage and neurodegenerative diseases. *Neural Regen Res*. 2013;8(21):2003–2014. doi:10.3969/j.issn.1673-5374.2013.21.009